Supplementary Materials

Spiral wheel with a reconfigurable shape and variable grip for all-terrain robots

Pan He, Hao Wang, Panding Wang, Hongshuai Lei, Shengyu Duan*, Zeang Zhao*

Institute of Advanced Structure Technology, Beijing Institute of Technology, Beijing 100081, China.

***Correspondence to:** Prof. Zeang Zhao, Prof. Shengyu Duan, Institute of Advanced Structure Technology, Beijing Institute of Technology, Beijing 100081, China. E-mail: zza@pku.edu.cn; syduan@bit.edu.cn

This PDF file includes:

Supplementary Texts 1 to 14

Supplementary Figures 1 to 20

Supplementary Tables 1 to 2

Supplementary Movies 1 to 11

Supplementary Text

Supplementary Text 1: The definition of obstacle-crossing capability

The formula for calculating the robot's obstacle-crossing capability is given in Equation (1), where M_{robot} represents the total weight of the robot, g is the gravitational acceleration, H_{max} is the maximum height the robot can overcome, n is the number of drive motors, and T_{max} is the maximum driving torque. The denominator of the equation represents the total sum of the driving torques, which is the product of the number of drive motors and their respective driving torques, while the numerator represents the product of the robot's weight and the maximum obstacle height it can overcome. This ratio is a dimensionless number that reflects the efficiency of driving torque utilization during the obstacle-crossing process. A higher ratio indicates that, under the same load and driving torque, the robot can overcome higher obstacles, implying stronger obstacle-crossing capability.

$$E_{\text{capability}} = \frac{M_{\text{robot}} g H_{\max}}{n T_{\max}} \quad (1)$$

Supplementary Text 2: The definition of the unevenness after the wheel contraction

The formula for calculating the unevenness of the outer rim after wheel contraction is shown in Equation (2), where R_{max} represents the maximum distance from a point on the outer rim to the wheel's center, and R_{min} represents the minimum distance. The unevenness of the outer rim after contraction is expressed as the ratio of the difference to the sum of these two values. A smaller ratio indicates that after contraction, the outer rim is closer to a perfect circle, with R_{max} and R_{min} being more similar.

$$Unevenness = \frac{R_{\max} - R_{\min}}{R_{\max} + R_{\min}} \quad (2)$$

Supplementary Text 3: Calculation methods for the grounding coefficient and average grounding pressure

The calculation formula for the ground contact coefficient of the wheel under radial load is shown in Equation (3)[1], where L_c represents the contact length and L_k represents the contact width. A higher ground contact coefficient results in increased longitudinal traction, improving acceleration and braking efficiency, making it particularly suitable for off-road or soft terrains, this coefficient has a substantial impact on the robot's obstacle-crossing capability. As for the average contact pressure, it is determined by averaging the pressures extracted from all the nodes, as shown in Equation (4), where N_{node} is the number of nodes extracted in the simulation, P_i is the contact pressure at node *i*.

$$K = \frac{L_c}{L_k} \tag{3}$$

$$\overline{P} = \frac{\sum_{i=1}^{N_{node}} P_i}{N_{node}} \tag{4}$$

Supplementary Text 4: Design of the spiral wheel's contraction mechanism

The spiral wheel's drive mechanism is shown in Figure S7(A). The system includes a 12V lithium battery, two brushless DC motors, and the necessary components for motor control. The motors have a maximum output torque of 1.8 N·m and a rated voltage of 12V. The mechanism is controlled by an ESP32 microcontroller and an L298N motor driver module, with control commands transmitted via Bluetooth. The ESP32 functions as both a transmitter and receiver for Bluetooth signals, maintaining a continuous Bluetooth connection with the main control unit during the robot's operation. In different driving conditions, the main control unit sends signals to the microcontroller to control the motor's direction and duration of rotation, enabling the switching between different spiral wheel configurations. The assembly process of the spiral wheel and its contraction mechanism with the robot is shown in Figure S8. There is an interference fit between the spiral wheel and the hub motor of the robot, while the drive mechanism is securely fixed to the hub motor using screws.

Supplementary Text 5: Simulation parameters for the spiral wheel

The material used for the spiral wheel is TPU83, a rubbery material. To obtain its constitutive model, uniaxial tensile testing was conducted to generate the corresponding stress-strain curve. Prior to the experiments, standard tensile specimens made of TPU83 material were fabricated according to existing standards and specifications. The structural dimensions of these specimens, as well as the model, are shown in Supplementary Material Figure S9(B). The tensile specimens were placed in a mechanical testing machine, as depicted in Figure S9(A), and an external video extensometer was used to measure displacement changes during the tensile process. By tracking the distance changes between characteristic points on the specimen's surface, deformation data can be generated. By combining the data from the force sensor on the testing machine and the specimen's cross-sectional area, the nominal stress-strain curve for the tensile specimen was further calculated. The resulting stress-strain data for the uniaxial tensile test of the standard specimen is shown in Figure S9(C). These data were then imported into Abaqus, where the software's material fitting tools were used to derive the appropriate constitutive model. These tools allow for fitting the selected strain energy function using the experimental data. The material's nominal stress-strain data obtained in this experiment were fitted to several models in Abaqus, including Mooney-Rivlin, Polynomial (N=2), Ogden, Neo Hooke, and Yeoh. The fitting comparison curves are shown in Figure S9(D). From the results, it is clear that the test data closely aligns with the Mooney-Rivlin model. Therefore, the Mooney-Rivlin model was selected, and the resulting parameters were used for simulation. For the Mooney-Rivlin constitutive model, the strain energy function is given by Equation (5)[2,3], where C_{10} = 0.0182, C_{01} = 2.834, and D_1= 0.

$$\mathrm{W} = C_{10}\left(I_1 - 3\right) + C_{01}\left(I_2 - 3\right) + \frac{1}{D_1}\left(\mathrm{J\text{-}1}\right)^2 \quad (5)$$

Supplementary Text 6: Measure of the rotational speed of the motor during the contraction process

The motor's rotational speed was obtained by counting the number of pulses received by the motor per unit of time. Each complete revolution of the motor's rotor generates 9 pulse signals. Since the motor and its gearbox are integrated with a reduction ratio of 506:1, after the motor's rotor completes 506 rotations, the visible output shaft of the motor completes one full rotation. Therefore, by dividing the number of pulses obtained in a given time interval by the corresponding factor, the rotational speed of the motor shaft can be calculated. The formula for this calculation is given in Equation (6), where num_{cal} represents the calculated number of feedback pulses from the motor, num_{base} is the number of pulses generated by one complete rotation of the motor's rotor, i_1 is the reduction ratio of the gearbox, Δt is the unit measurement time, and n_{shaft} is the calculated rotational speed of the motor shaft. For calculating num_{cal}, an interrupt counting method using a microcontroller is employed. Each pulse corresponds to a high voltage signal. The motor's feedback pulse voltage data line is connected to a pin on the microcontroller. Every time this pin receives a high voltage signal, an interrupt is triggered, and the pulse count is incremented by 1. The unit measurement time for the interrupt program is set to 0.5 seconds. Once the pulse count is obtained, it is divided by the corresponding factor to calculate the motor shaft speed. The results of the rotational speed variation of the four motors in the spiral wheel contraction process are shown in Figure S5(B).

$$n_{shaft} = \frac{num_{cal}}{i_1 \cdot num_{base} \cdot \Delta t} \qquad (6)$$

After obtaining the relationship between the contraction motor speed and time, the motor's rotational angle over time was determined by integrating the speed, as shown in Figure S10(A). Motor 1 and 2 are contraction motors from the same contraction unit, controlling the wheels on one side of the robot, while Motor 3 and 4 control the wheels on the opposite side. Due to the robot's center of gravity not being perfectly aligned with the geometric center and the limitations of the manufacturing process, the resistances encountered by the two wheels during the contraction are not exactly the same. This results in slight differences in the angular changes of the motors in each unit during contraction. The software ImageJ was used to extract the rotation angle of a point on the edge of the spiral wheel around its center, as well as the

variation of the wheel's radius over time. Detailed instructions for using the software can be found in the Methods section of the main text. After specifying a reference length in the provided image, this tool can measure both the length and angle of lines formed by pixel points in the image. The relationship between the spiral wheel's edge rotation angle and its radius with respect to the contraction motor's rotation angle is shown in Figures S10(B) and S10(C). The relationship between the spiral wheel's radius and the edge rotation angle is depicted in Figure S10(D), indicating that the radius and edge rotation angle exhibit a nearly linear relationship.

Supplementary Text 7: The rigid wheel-based standing balance control method for robots

When the robot maintains an upright posture, the hip joint motors are locked to keep the leg linkage mechanism fixed. In this state, the robot can be effectively modeled as a two-wheeled self-balancing robot. With rigid wheels, a Linear Quadratic Regulator (LQR) is used to control the robot's balance and speed[4]. First, the spatial state equations of the robot are formulated, as shown in Equation (7):

$$\dot{x}(t) = Ax(t) + Bu(t) \qquad (7)$$

For the robot's balancing system, the speed, tilt angle, and tilt angular velocity are treated as state variables. As a result, the above equation can be transformed into the form shown in Equation (8). Here, x_b represents the x-coordinate of the contact point, with the x-axis indicating the robot's direction of travel; φ is the tilt angle of the robot's legs; and T_φ is the input torque.

$$\begin{bmatrix} \ddot{x}_b \\ \dot{\phi} \\ \ddot{\phi} \end{bmatrix} = \begin{bmatrix} A_{22} & A_{23} & 0 \\ 0 & 0 & 1 \\ A_{42} & A_{43} & 0 \end{bmatrix} \begin{bmatrix} \dot{x}_b \\ \phi \\ \dot{\phi} \end{bmatrix} + \begin{bmatrix} B_1 \\ 0 \\ B_2 \end{bmatrix} T_\phi \qquad (8)$$

In Equation (8), the following relationships hold, where M is the total weight of the robot, m_b is the weight of the robot excluding the wheels, r is the radius of the rigid wheel, L is the total length of the robot, b is the ground friction coefficient, I_w is the rotational inertia of the rigid wheel, I_b is the moment of inertia of the robot's body around the y-axis, and I_t is the moment of inertia of the robot's body around the z-axis.

$$\Delta = r^2(2M^2L^2 + 2m_bML^2 - 2m_bI_b - MI_b) + 2ML^2I_w - 2I_wI_b \quad (9)$$

$$A_{22} = 2(bML^2 - bI_b + MLrb)/\Delta \quad (10)$$

$$A_{23} = M^2gL^2r^2/\Delta \quad (11)$$

$$A_{42} = (4brm_b + 2Mbr + 4bI_w/r - 2MbL)/\Delta \quad (12)$$

$$A_{43} = (2Mm_bgLr^2 + M^2gLr^2 + 2I_wMgL)/\Delta \quad (13)$$

$$B_2 = (-ML^2r + I_br - MLr^2)/\Delta \quad (14)$$

$$B_4 = (-2m_br^2 - Mr^2 - 2I_w + MLr)/\Delta \quad (15)$$

$$B_6 = Dr/(D^2I_w + m_bD^2r^2 + 2I_tr^2) \quad (16)$$

$$B_1 = \begin{bmatrix} 0 \\ B_2 \\ 0 \\ B_4 \end{bmatrix} \quad (17) \qquad B_2 = \begin{bmatrix} 0 \\ B_6 \end{bmatrix} \quad (18)$$

When the robot maintains balance and travels at a speed of v_{ref}, the legs remain in a vertical position, resulting in a tilt angular velocity of zero. This leads to the relationships $x=v_{ref}$ and $\dot{\varphi}=0$. The system's steady-state variables are $x_s=F(v_{ref})$, and the steady-state control input is $u_s=G(v_{ref})$. By introducing new state variables $\Delta x=x-x_s$ and new system inputs $\Delta u=T_\varphi-u_s$, the new system state equations can be derived, as shown in Equation (19).

$$\dot{\Delta x} = \begin{bmatrix} A_{22} & A_{23} & 0 \\ 0 & 0 & 1 \\ A_{42} & A_{43} & 0 \end{bmatrix} \Delta x + \begin{bmatrix} B_1 \\ 0 \\ B_2 \end{bmatrix} \Delta u \quad (19)$$

The optimal control input can be obtained from Equation (20).

$$u = u_s - k\Delta x \quad (20)$$

The functions F and G are defined as follows:

$$F(v_{ref}) = \begin{bmatrix} v_{ref} \\ \dfrac{A_{22}B_2 - A_{42}B_1}{A_{43}B_1 - A_{23}B_2} \\ 0 \end{bmatrix} \quad (21)$$

$$G(v_{ref}) = \frac{A_{42}A_{23} - A_{22}A_{43}}{A_{43}B_1 - A_{23}B_2} \quad (22)$$

The optimal control gain matrix K is determined by solving the corresponding discrete-time algebraic Riccati equation, given by Equation (23), where Q and R are positive semi-definite weighting matrices. The resulting K is expressed in Equation (24).

$$P = A^T PA - A^T PB(R + B^T PB)^{-1} B^T PA + Q \quad (23)$$

$$K = R^{-1} B^T P \quad (24)$$

Supplementary Text 8: Energy consumption testing of the contraction mechanism and a comparison of the robot's energy consumption under different wheel configurations.

A quantitative analysis of energy consumption was conducted, and the energy consumption of the contraction mechanism was first analyzed. The contraction mechanism is powered by an independent lithium battery, which does not rely on the central power supply of the robot. To quantify energy consumption, this study employs a straightforward method by monitoring the battery voltage. The fully charged lithium battery has an output voltage of 12.3 V and a capacity of 2800 mAh. The mechanism was operated repeatedly to switch the flexible wheel between its fully expanded and contracted states. The number of switching cycles and the corresponding battery output voltage were recorded during operation. The results, shown in Figure S13(A), demonstrate a linear decrease in the output voltage of the battery as the number of switches increases. After 100 expansion-contraction cycles, the battery voltage decreased from 12.3V to 10.8V. The discharge process of the lithium battery follows a constant current discharge characteristic, as depicted in Figure S13(B). With an output current of 1A, the battery voltage rapidly drops to 0V once the output voltage reaches 8.5V, indicating complete depletion of the battery's energy. During discharge, the battery's voltage decreases linearly with energy consumption. The area enclosed by the curve and the horizontal axis represents the energy consumed. At an output voltage of 10.8V, the battery has not yet been fully depleted. The total energy capacity of the battery is approximately 22.8Wh (82.1kJ), as provided by the manufacturer. Therefore, it can be inferred that the energy consumed per switch during the 100 cycles is less than 0.821kJ.

For the energy consumption testing of the robot during travel in different wheel configurations, a similar approach was employed to measure the relationship between the output voltage of the robot's power supply and the travel distance. The results are presented in Figure S13(C). A flat concrete surface was selected as the driving environment for this experiment, as it provides better control over environmental consistency compared to terrains such as grass, thus minimizing the impact of unknown variables. The robot's motors were set to operate at maximum power throughout the experiment. The results show that with the wheels in the expanded state, the robot's maximum travel distance was 2.5 km, at which point the battery's output voltage dropped sharply to 5.7V. In contrast, with the wheels in the contracted state, the maximum travel distance increased to 4.4 km. This represents an obvious improvement in energy efficiency, with the contracted wheel state achieving approximately 1.76 times better energy utilization. These results confirm the validity of the initial design concept, wherein the expanded wheel state is employed for obstacle traversal, while the contracted state is optimized for low-energy, high-speed travel.

Supplementary Text 9: Fatigue and wear testing of wheel materials.

To assess the reliability of the wheel structure, fatigue and wear tests were conducted. The fatigue properties of the TPU83 material were used to assess the overall fatigue behavior of the structure, given the limitations of the experimental equipment. The region experiencing the highest alternating stress within the wheel structure is the outer rim. As detailed in the main text, the contract simulation was employed to determine that the maximum local stress at the outer rim is 1 MPa. Based on this stress value, uniaxial tensile fatigue testing was performed on the material, as illustrated in Figure S14(A). During the fatigue tests, triangular wave loading was applied to the sample, with a peak stress of 1 MPa and a stress ratio of 0.1 between the minimum and maximum stresses. Considering that the entire shape-switching cycle of the wheel takes approximately 28 seconds, around two shape changes occur per minute. To ensure safety, the loading frequency for the fatigue test was set to three cycles per minute, for a total of 1000 cycles. The results, presented in Figure S14(B), show that after 1000 loading cycles, the test sample exhibited no significant

plastic deformation or crack formation. The initial length of the sample was 170 mm, and after the test, its measured length remains approximately 170 mm, confirming that the use of this material in the design is both reasonable and reliable.

The wear characteristics of the wheel were also evaluated based on the material's wear properties. Initially, a standard friction specimen was developed, and reciprocating friction tests were conducted to analyze wear parameters. The spherical contact friction method was employed during the experiment, utilizing a 5 mm diameter ball made of silicon nitride. Prior to the experiment, it was necessary to determine the force exerted on the friction head during the friction process. As analyzed in the main text, the contact pressure when the wheel interacts with the ground was found to be highest when the wheel is in the contracted state, reaching 1.2 MPa. Based on this contact pressure, the pressure exerted by the friction head on the flat surface of the specimen was maintained at this level. To calculate the required force on the friction head to sustain this contact pressure, finite element simulation was implemented. The setup for the contact simulation is shown in Figure S15(A). When an applied force of 0.8 N was used, the resulting contact simulation, shown in Figure S15(B), indicated that the average pressure within the contact area approached 1.2 MPa.

The test was first conducted under typical driving conditions, applying a force of 0.8 N to the friction head, with a test distance of 10 mm and 43,200 friction cycles. After completing the friction test, 3D profilometry scans were performed on the sample to measure its volume loss. The results of the 3D scan under typical driving conditions are shown in Figure S15(C), where the surface of the specimen was sampled at various points. Based on these measurements, the depth of the wear marks was calculated, as depicted in Figure S15(D). This graph illustrates the variation in wear depth across the width direction in the middle region of the specimen. The results indicate that the maximum wear depth did not exceed 50μm. Due to the minimal wear, which was below the resolution capacity of the scanning device, the wear volume could not be accurately calculated. In addition to the test under typical driving conditions, wear was also tested under more severe and complex driving environments. For scenarios involving intense contact, such as collisions and obstacle crossings, the force on the friction head was increased to 5 N, while maintaining the same number of friction cycles and distance. The wear test results, followed by 3D profilometry scans of the specimen, are presented in Figure S15(E). The 3D scan

results showed a wear volume of 0.628 mm^3, which is very small relative to the overall volume. Furthermore, mass loss before and after the test was compared, as shown in Figures S15(F) and S15(G). The initial mass was 15.512 g, and the post-test mass was 15.502 g, resulting in a mass loss of 0.010 g, or approximately 0.061% of the original mass—an extremely small reduction. The depth of the wear marks along the width direction of the middle region of the specimen after wear is shown in Figure S15(H). The results indicate that increasing the force to 5 N led to a wear mark depth of up to 120μm, but the overall wear volume remained minimal. The friction test results demonstrate that the use of TPU83 as the material for the proposed wheel design is both reasonable and reliable.

Supplementary Text 10: Analysis of the motion performance of the wheel in its intermediate state.

The stiffness of the wheel at different intermediate states was tested. The wheel was mounted on a test bench during the experiment, and the driving mechanism was employed to contract the wheel to various diameters. Compression tests were performed, and displacement-load curves were obtained to analyze the variation in stiffness, with the results presented in Figure S16(A). The results indicate that during the initial phase of diameter reduction, the radial stiffness of the wheel remains relatively unchanged. However, once the diameter reaches 30 mm, an obvious increase in radial stiffness is observed. This can be attributed to the fact that, during the early stages of contraction, the gaps between the spokes are not fully compressed, leaving considerable space between them. The radial stiffness of the wheel has a direct influence on the contact deformation with obstacles. In the expanded state, the wheel's ability to overcome obstacles is primarily based on its inherent flexibility, allowing it to deform upon contact and adapt to the contours of the obstacles, thus preventing it from becoming stuck during movement. As the diameter decreases in the later stages, the stiffness increases sharply, leading to a marked reduction in contact deformation. At this point, the wheel behaves similarly to a conventional rigid wheel. Based on the analysis of the stiffness variation above, further performance analysis of the wheel's intermediate states was conducted. From the perspective of speed and driving stability, the tighter the wheel contracts, the closer its performance is to that of

a traditional rigid wheel. This results in lower rolling resistance and higher stability. As shown in the experimental results in Figure 3C, the ride roughness corresponding to the fully contracted state of the wheel is remarkably smaller than that in the expanded state. Therefore, if speed and stability are prioritized, the fully contracted state is the best choice. From the perspective of obstacle-crossing capability, although there is no obvious change in radial stiffness during the initial phase of diameter reduction, one critical parameter is changing—the ratio of the wheel's radius to the vertical height of the obstacle. The larger the radius of the wheel relative to the obstacle height, the easier it is to cross the obstacle[5–7]. In vehicle dynamics, for a given wheel's radius, the maximum obstacle-crossing height generally follows the universal relationship shown in Equation (25)[8],

$$h_0 = r - h_{zs} - (r - h_n)\mu \qquad (25)$$

where r is the wheel's radius, h_{zs} is the soil penetration depth, h_n is the deformation of the wheel at the obstacle edge, μ is determined by the load on the wheel and the manner in which it contacts the obstacle. In the same robot and driving scenario, the main parameters determining the maximum obstacle-crossing height are the wheel radius and edge contact deformation. During the early stages of the wheel's shape change, since stiffness variation is minimal, it can be assumed that the contact deformation remains approximately constant. Thus, the only factor determining the obstacle-crossing limit is the wheel's radius. When the wheel is in its fully expanded state, the radius is maximized, and its obstacle-crossing capability is strongest. Therefore, using this configuration for obstacle-crossing is the optimal choice. Considering the control complexity and the work we plan to carry out in the next phase, our research focuses only on the two extreme states of the wheel. This decision minimizes other development issues while ensuring practical applicability.

Supplementary Text 11: Analysis of the scalability and generalizability of the wheel design.

Analysis of the scalability and generalizability of the wheel design was also conducted in this study. The original wheel featured a central mounting hole diameter of 144 mm, an outer diameter of 412 mm, a spoke thickness of 6.5 mm, and 28 spokes.

To examine its scalability, all parameters except the central mounting hole diameter and outer diameter were kept constant. These two dimensions were varied as they represent the size of the platform on which the wheel can be mounted and the size of the wheel itself. Given the substantial time and economic costs associated with physical manufacturing, finite element simulation methods were employed for validation. In the simulation, the central mounting hole diameters were set to 104 mm, 144 mm, and 184 mm, with corresponding outer diameters of 372 mm, 412 mm, and 452 mm. The results, presented in Figures S17 to S19, indicate that for wheels with varying mounting and structural dimensions, both the feasibility of shape transitions and the stiffness variation before and after shape adjustments yield reasonable outcomes. For other mobile platforms, appropriate adjustments to the overall structural and mounting dimensions can achieve the desired performance.

Supplementary Text 12: Selection of rope material and analysis of strength and wear resistance.

The driving force required to alter the configuration of the wheel is first estimated using simulation methods, as detailed in the Materials and Methods section. To drive the wheel's contraction, pressure is applied in the fixed area of the spokes within the simulation. For a wheel with a spoke thickness of 6.5mm, 28 spokes, and an outer ring thickness of 2mm, the minimum pressure necessary to achieve full contraction is found through simulation to be 0.014 MPa. The pressure application area is approximately 22mm in length and 52mm in width (equivalent to the wheel thickness), resulting in an area of 1144 mm^2. Based on this, the estimated force exerted by the rope on each spoke is around 16N. Given that a single motor drives the contraction of 14 spokes, the total pulling force required from one motor is approximately 224N. Considering the need for the rope to possess high strength, excellent wear resistance, and other critical properties, while maintaining an economical cost, commercially available nylon ropes were selected. Stretching tests were conducted on several nylon ropes of different diameters, and the results are presented in Figure S20(A). Due to the rope's structure being composed of fluffy fibers, it becomes more compact after a period of stretching, causing the tangential stiffness to slightly increase during the latter half of the stretch. However, the entire process remains elastic. As indicated in

the figure, the 1.5mm diameter rope failed under a load of less than 200N, making it unsuitable for the driving mechanism. Conversely, the 2mm and 2.5mm diameter ropes require breaking forces exceeding 300N, which are theoretically within the safe range. However, due to the limited size of the winding pulley, larger diameter ropes would require a larger winding pulley. Therefore, a 2mm diameter nylon rope was selected in the final design.

Rope wear was considered during the design phase. As illustrated in Figure S20(B), a cross-sectional analysis of the wheel reveals a distinct spatial distribution of the rope's path, indicated by the yellow markings on the spokes. This trajectory helps prevent excessive bending of the rope, which would otherwise increase friction. This design effectively mitigates the adverse effects of friction. During testing, however, obvious wear was observed in certain localized areas. In response, isolating pad sleeves were added in these high-friction regions to prevent direct contact between the rope and the wheel. These sleeves are fabricated from high-strength, wear-resistant material, which substantially reduces wear between the rope and the wheel. In summary, both the strength and wear resistance of the rope were thoroughly addressed during the design phase to ensure the proper functioning of the mechanism.

Supplementary Text 13: Motor control process.

After obtaining the results of the motor speed variation during the contraction process (as shown in Figure S5(A)), it can be observed that the motor speed approaches approximately 0.06 r/s at the end of contraction. Accordingly, this value is adopted as the threshold for motor speed control in this study to regulate the motor's start and stop. The motor control flow is illustrated in Figure S5(B): the microcontroller in the contraction mechanism receives different signals and executes corresponding actions. During the motor's forward rotation, the speed threshold is employed to determine whether the motor needs to stop. If the speed drops below this threshold, the motor is deemed overloaded and stops immediately. During reverse rotation, a time threshold is used to judge the motor's stop condition; if the rotation time exceeds this threshold, the motor power is cut off, and the motor ceases operation.

Supplementary Text 14: Analysis of vibration test results for the wheel in expanded state during forward and reverse travel

In the expanded state, the Z-axis acceleration in the forward direction is substantially higher than in the reverse direction. The Z-axis acceleration for forward motion is distributed within ±20 m/s², while for reverse motion, the values are similar to those in the contracted state, ranging within ±5 m/s². The noticeable difference in Z-axis acceleration between forward and reverse motion at full speed in the expanded state is manifested as much greater bumpiness during forward motion compared to reverse motion. The cause of this difference lies primarily in the rotational direction of the spiral wheel's outer teeth. During forward motion, the ground reaction force opposes the direction of the teeth's rotation, leading to a complex deformation phase during the wheel-ground contact. This results in a larger excitation force transmitted to the robot system, whereas in reverse motion, the ground reaction force aligns with the rotation direction of the teeth, generating smaller excitation forces and, consequently, less bumpiness. Although forward motion at high speeds exhibits greater bumpiness, the interaction between the wheel teeth and the ground is more conducive to obstacle negotiation, since obstacle traversal typically occurs at low speeds. This result has practical implications for subsequent motion control; for example, with the spiral wheel in its expanded state, forward motion can be fully utilized for obstacle traversal, while reverse motion can be employed to navigate through relatively flat terrain between obstacles.

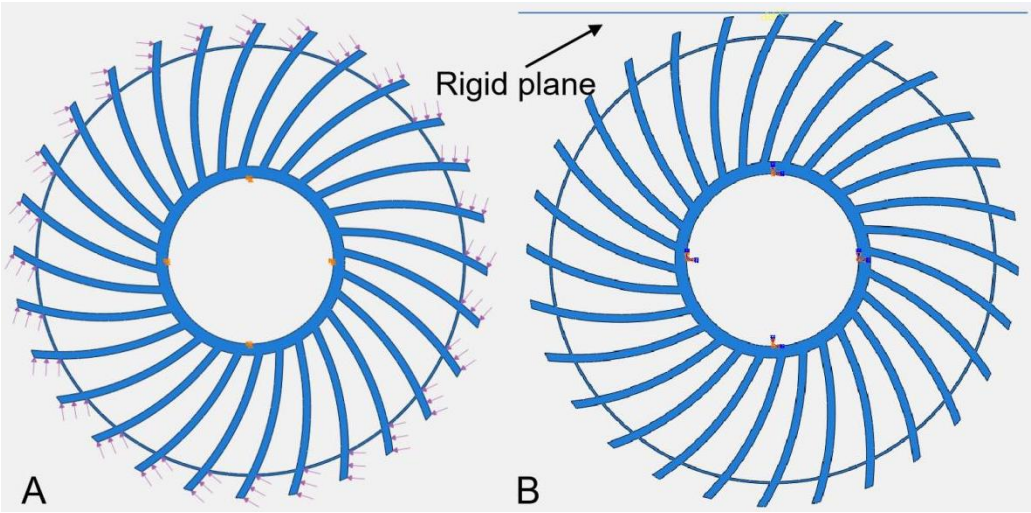

Supplementary Figure 1. Simulation models for contraction and radial compression of the spiral wheel. (A) Simulation method for the contraction of the spiral wheel: Six degrees of freedom at the center hole of the spiral wheel are fixed, and a uniform pressure is applied at the same position along each wheel spoke. (B) Simulation method for radial compression of the spiral wheel: Six degrees of freedom at the center hole are fixed, a reference point is coupled with a rigid plane, and displacement loading is applied at this reference point.

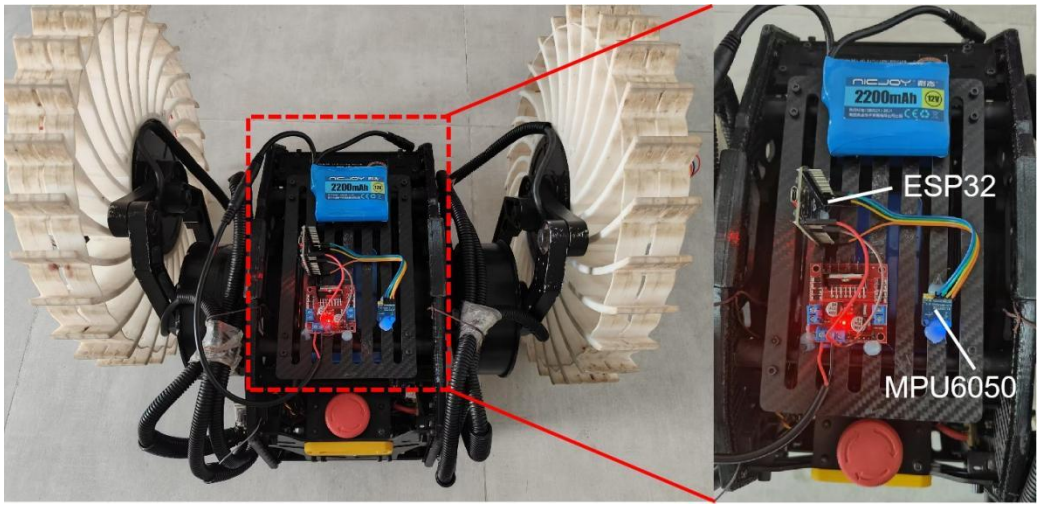

Supplementary Figure 2. Measurement method for Z-axis acceleration during movement. The MPU6050 inertial sensor is mounted on the top of the robot and powered independently. Using the built-in Bluetooth communication feature of the ESP32 microcontroller, the data collected by the sensor is transmitted to the display terminal.(Photographed by the authors).

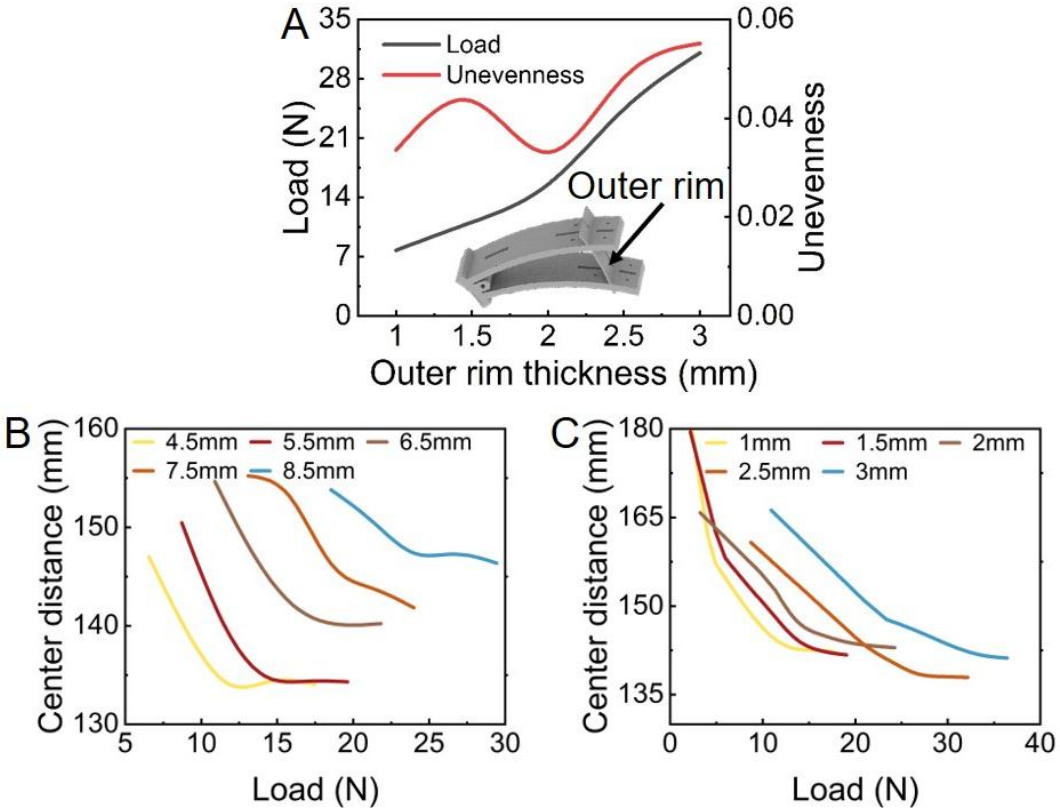

Supplementary Figure 3. Study on the structural parameters of the spiral wheel. (A) The effect of the outer rim thickness of the spiral wheel on the external force required for wheel contraction and the unevenness of the outer rim after contraction. (B) The effect of the external force on the contraction degree of the spiral wheel with different spoke thicknesses. (C) The effect of the external force on the contraction degree of the spiral wheel with different outer rim thicknesses.

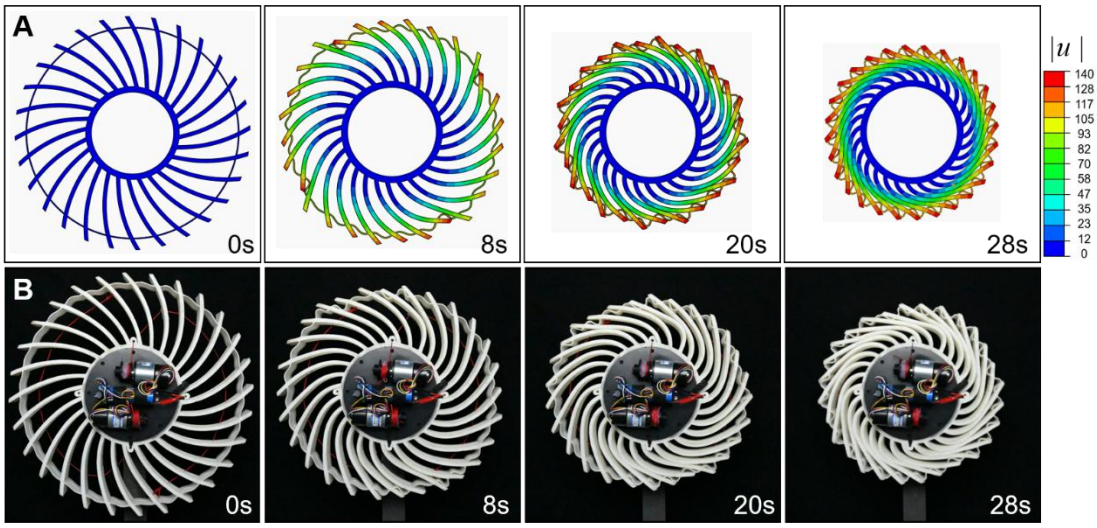

Supplementary Figure 4. Spiral wheel contraction simulation and experiment. (A) Simulation results of spiral wheel contraction. (B) Experimental results of spiral wheel contraction(Photographed by the authors).

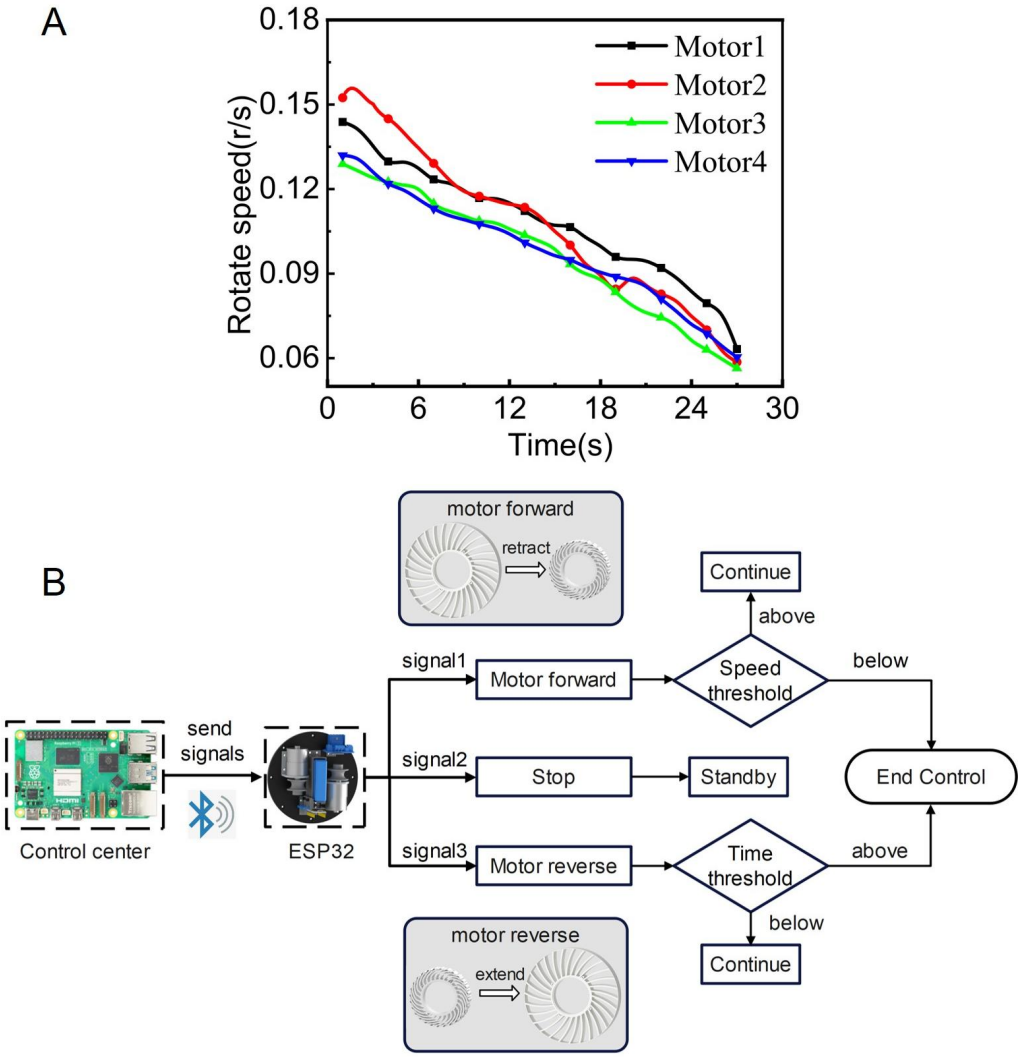

Supplementary Figure 5. Control process and speed measurement of the contraction motor. (A) Speed measurement of the motor during the contraction of the spiral wheel. (B) Control flow of the motor.

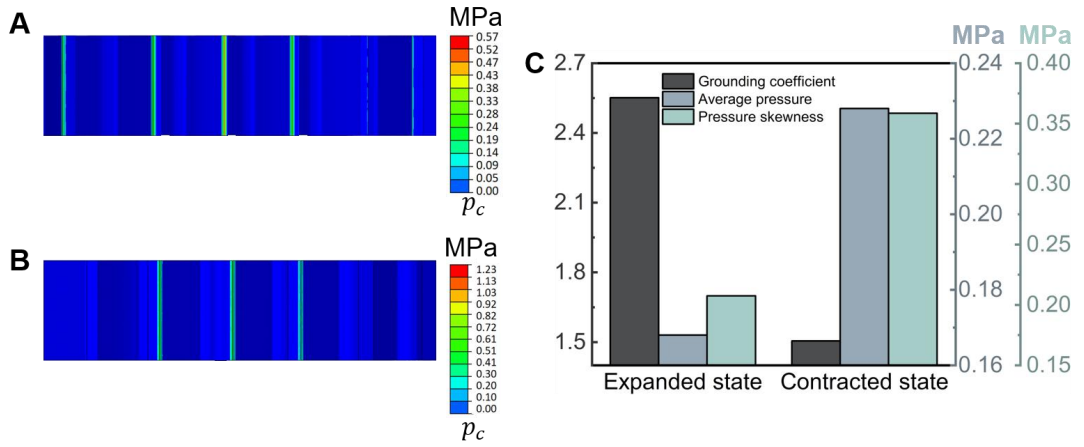

Supplementary Figure 6. Grounding parameter results of the spiral wheel mounted on the robot. (A) Ground pressure distribution contour map of the spiral wheel in the expanded state. (B) Ground pressure distribution contour map of the spiral wheel in the contracted state. (C) Grounding parameter results of the spiral wheel.

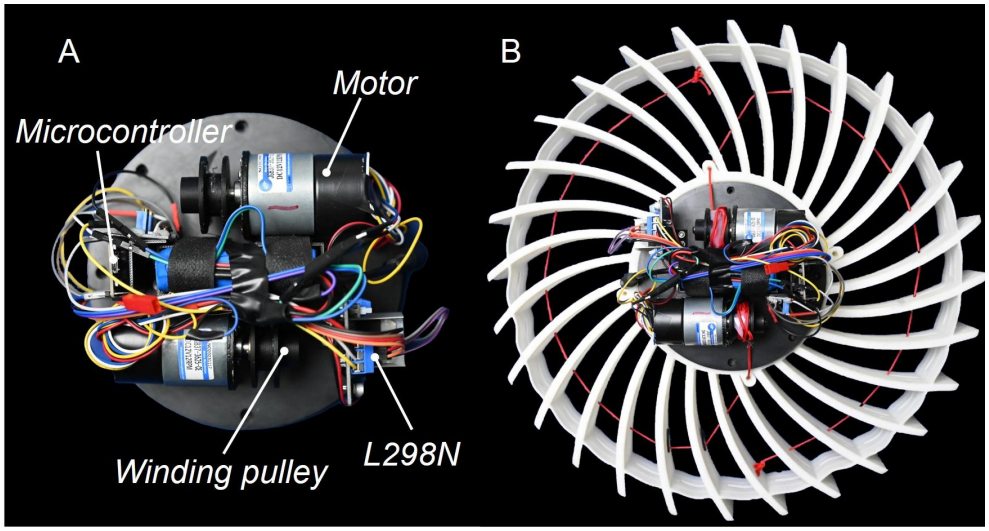

Supplementary Figure 7. Spiral wheel and its contraction mechanism. (A) The contraction mechanism of the spiral wheel, which primarily includes a contraction motor, a winding pulley, a lithium battery, and a control microcontroller (ESP32)(Photographed by the authors). (B) An assembled view of the contraction mechanism and the spiral wheel, where the force from the motor in the mechanism is transmitted to the spiral wheel via a fine rope. (Photographed by the authors).

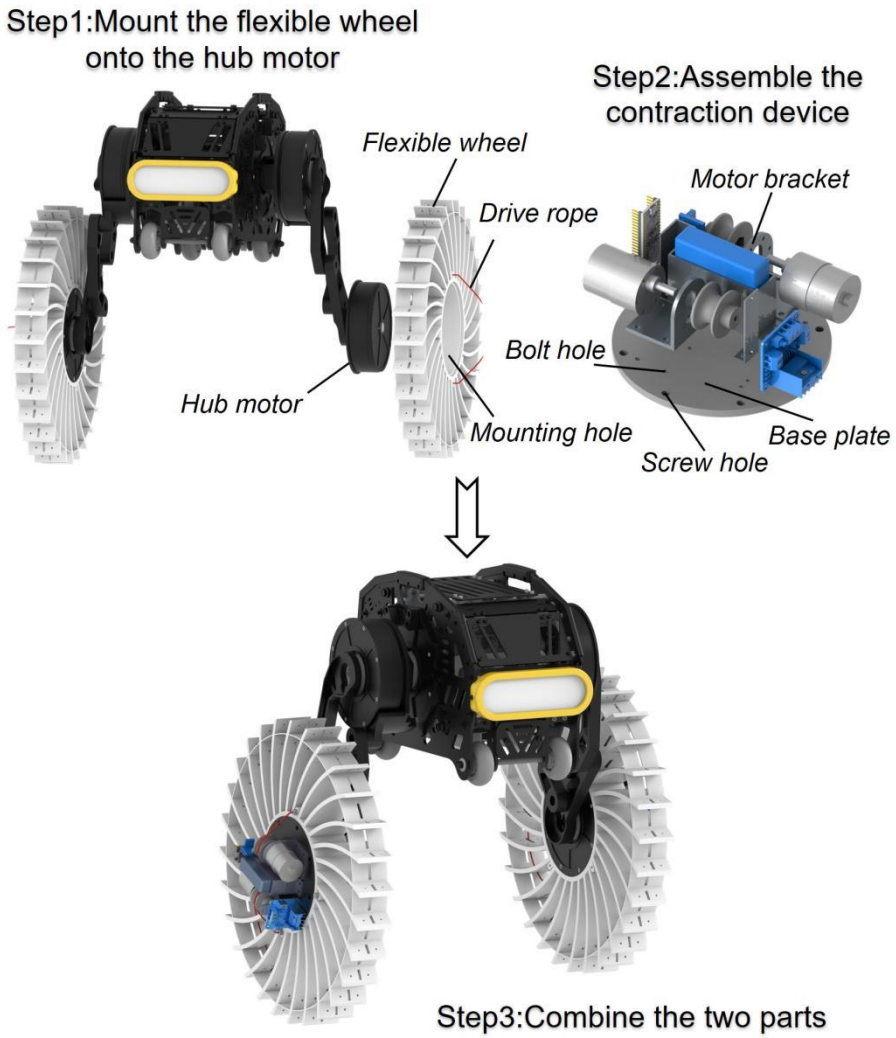

Supplementary Figure 8. Installation process of the spiral wheel and robot. The installation process consists of three main steps. The first step is to mount the spiral wheel onto the hub motor. The installation hole of the spiral wheel and the hub motor are press-fitted, effectively preventing relative slippage between the wheel and the motor. The second step involves assembling the contraction device. The components inside the contraction device are secured to the base plate using bolts and nuts, while the base plate is fixed to the hub motor with screws. The installation between the base plate and the hub motor also helps to compress and prevent slipping of the spiral wheel. The third step is to combine the two previously assembled parts, resulting in a fully integrated robot with the spiral wheel.

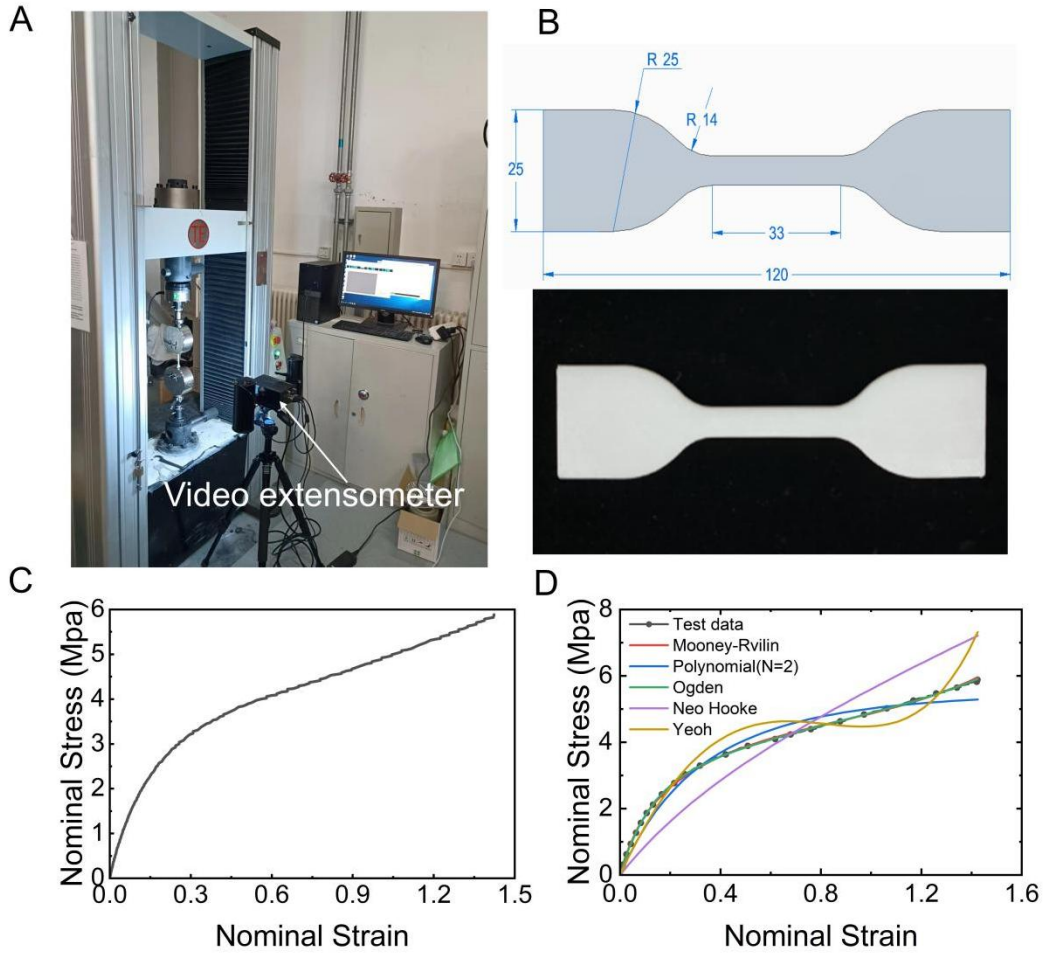

Supplementary Figure 9. Experimental measurement of the constitutive model for TPU83 material. (A) Uniaxial tensile testing of TPU standard specimens on a testing machine, combined with a video extensometer(Photographed by the authors). (B) Model dimensions and physical appearance of the standard specimens. (C) Nominal stress-strain curve obtained from the uniaxial tensile test of the standard specimens. (D) Fitting results of experimental data using various constitutive models in Abaqus. The Mooney-Rivlin model was found to best match the experimental data, and the material parameters determined from this model were used for subsequent simulations.

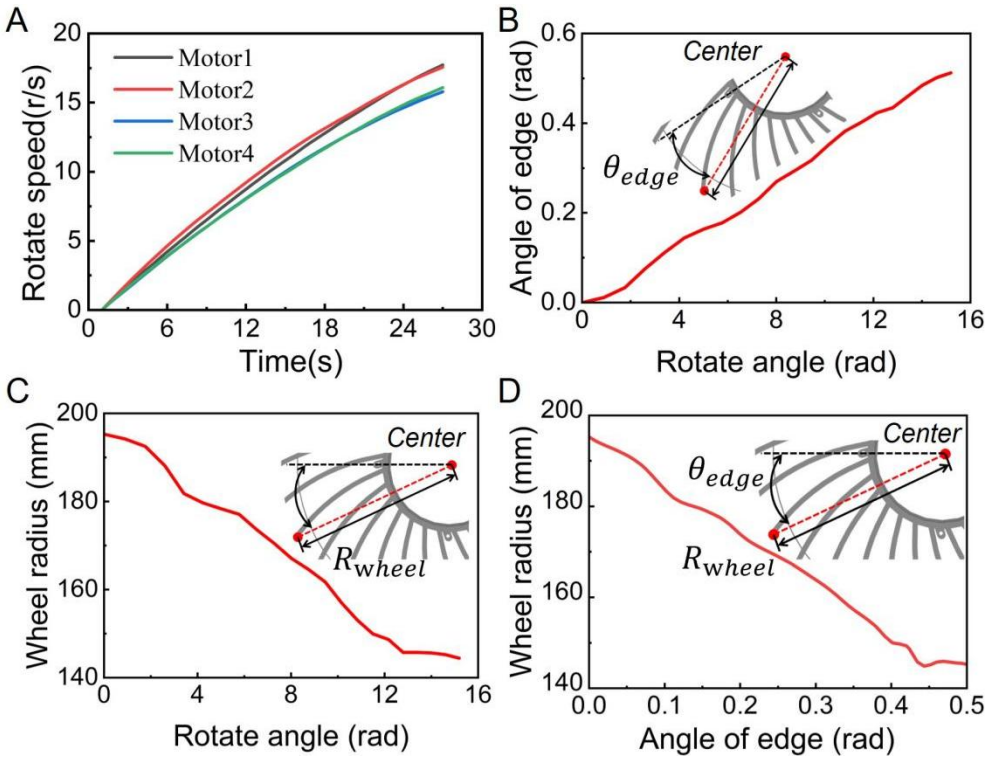

Supplementary Figure 10. Variation of the contraction motor's angle over time and the relationship between the spiral wheel radius and edge angle. (A) The change in the motor angles over time during the contraction process for the four motors. (B) The relationship between the edge angle of the spiral wheel and the contraction motor angle. (C) The relationship between the radius of the spiral wheel and the contraction motor angle. (D) The relationship between the radius of the spiral wheel and the edge angle.

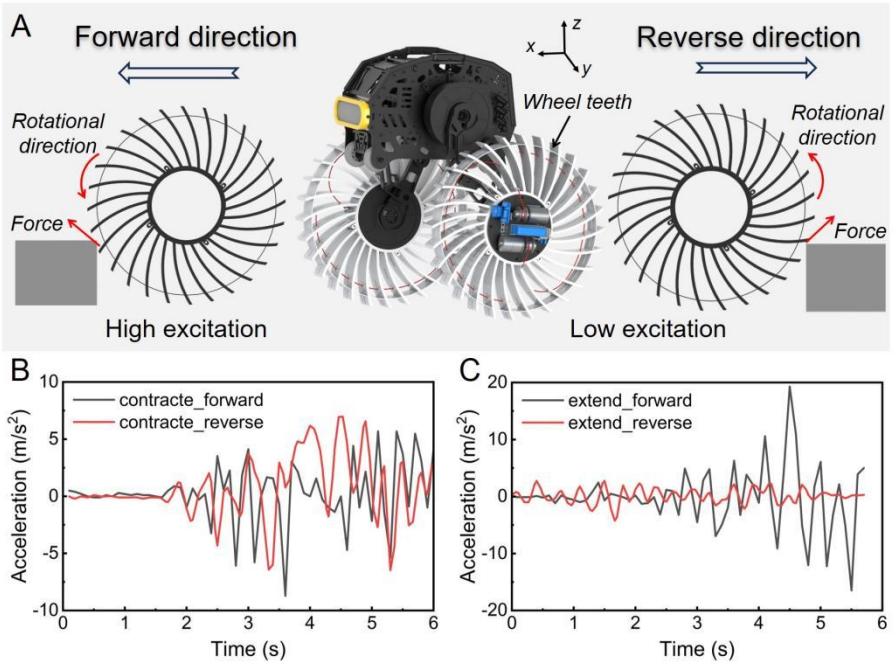

Supplementary Figure 11. Measurement of Z-axis acceleration during full-speed forward and reverse motion of the robot with the spiral wheel. (A) The relationship between the robot's forward and reverse motion directions, the ground reaction force direction, and the rotational direction of the spiral wheel's teeth during forward and reverse travel. (B) Z-axis acceleration during forward and reverse motion with the spiral wheel in its contracted state. In the contracted state, there is no noticeable difference in the Z-axis acceleration between the two motion directions, with the acceleration distributed within ±5 m/s². (C) Z-axis acceleration during forward and reverse motion with the spiral wheel in its expanded state.

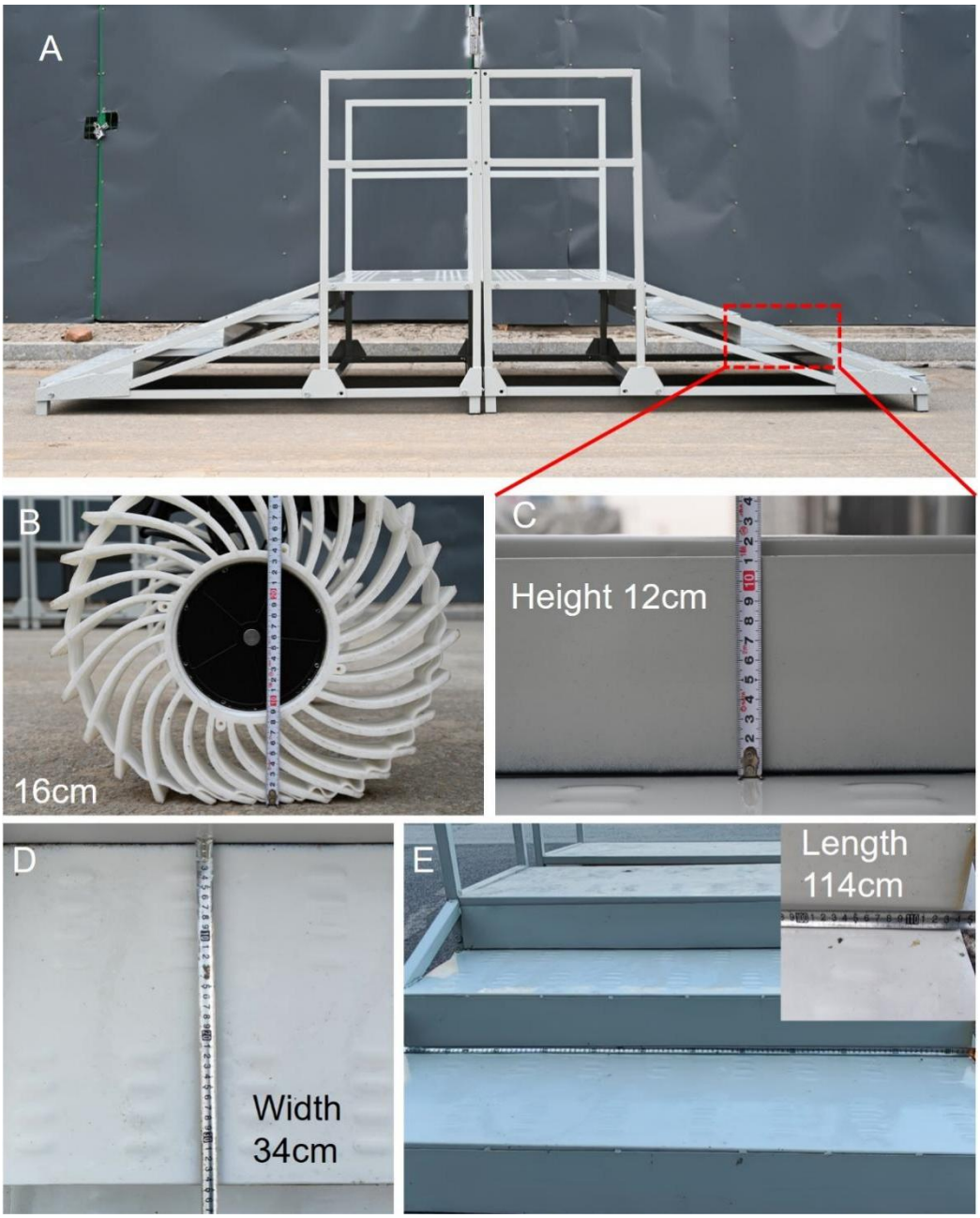

Supplementary Figure 12. Experimental setup for robot stair climbing. (A) Stairs used for the robot climbing experiment. The stairs are symmetric, with three steps each for both the ascent and descent sections. (B) The wheel hub height above the ground after the spiral wheel is installed is 16 cm. (C) The height of a single step is 12 cm. (D) The width of a single step is 34 cm. (E) The length of a single step is 114 cm.(Photographed by the authors.)

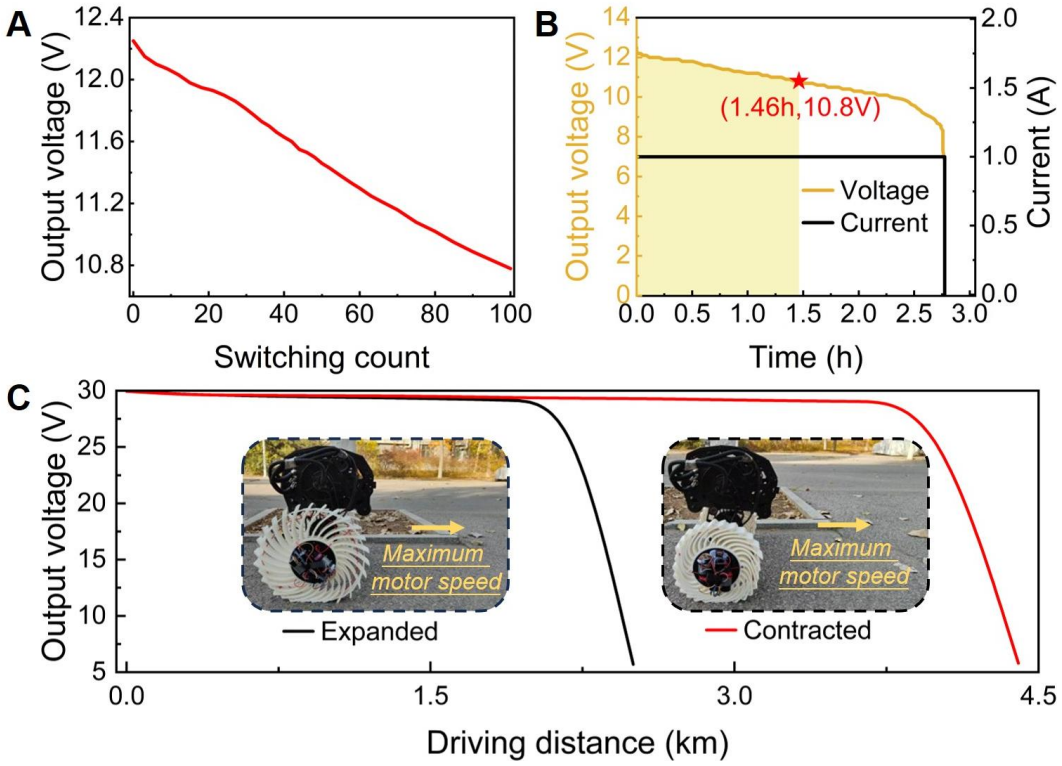

Supplementary Figure 13. Energy consumption analysis during wheel configuration switching and travel in different states. (A) Relationship between the output voltage of the lithium battery in the contraction mechanism and the number of wheel configuration switches. (B)According to the data provided by the manufacturer, the relationship between the output voltage of the lithium battery and its operating time in the contraction mechanism. (C) Comparison of the robot's maximum travel distance at full speed with the flexible wheel in the expanded and contracted states(Photographed by the authors).

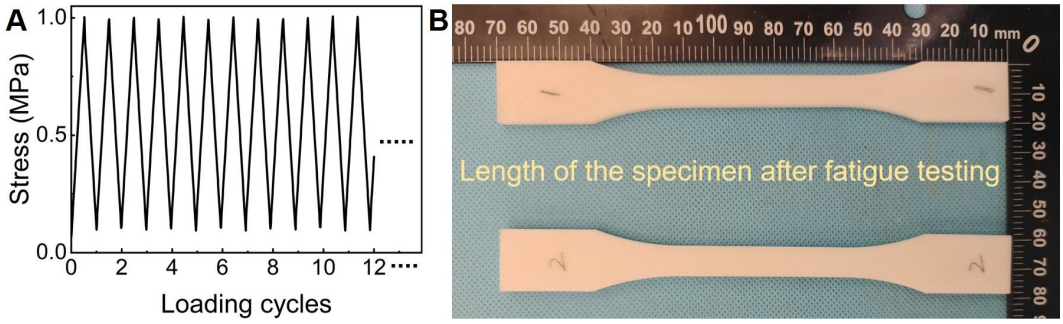

Supplementary Figure 14. Fatigue testing stress loading method and length of the specimen after testing. (A) The fatigue test employs a triangular wave stress loading method, with a total of 1,000 loading cycles applied. (B) The length of the specimen after undergoing fatigue testing(Photographed by the authors).

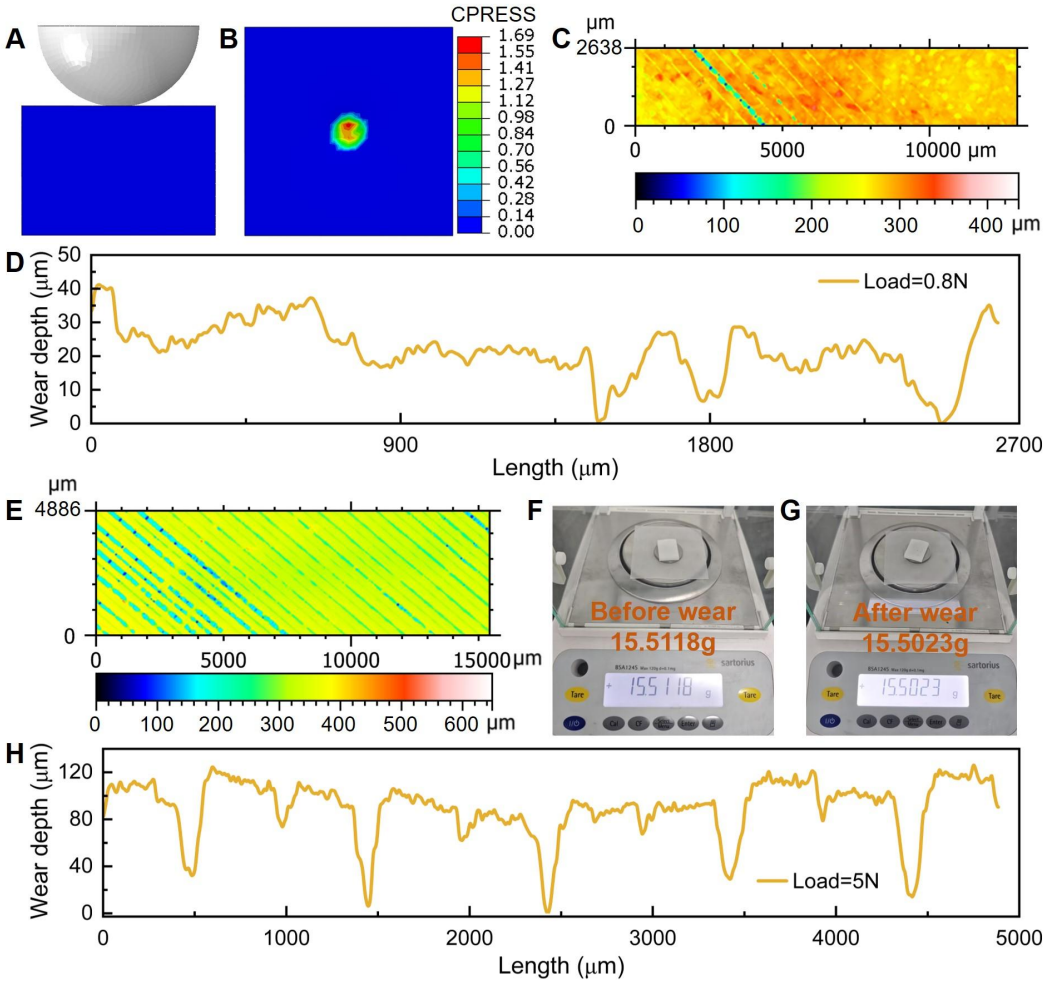

Supplementary Figure 15. Simulation and experimental results of the wear tests. (A) Simulation setup in Abaqus for calculating the required force on the friction head during the experiment. (B) Simulation results for calculating the force to be applied on the friction head. (C) 3D profilometry scan of the specimen after the wear test under a force of 0.8 N on the friction head. (D) Variation in wear depth across the width direction in the middle region of the specimen after the 0.8 N wear test. (E) 3D profilometry scan of the specimen after the wear test under a force of 5 N on the friction head. (F) Mass of the specimen before the 5 N wear test(Photographed by the authors.). (G) Mass of the specimen after the 5 N wear test(Photographed by the authors.). (H) Variation in wear depth across the width direction in the middle region of the specimen after the 5 N wear test.

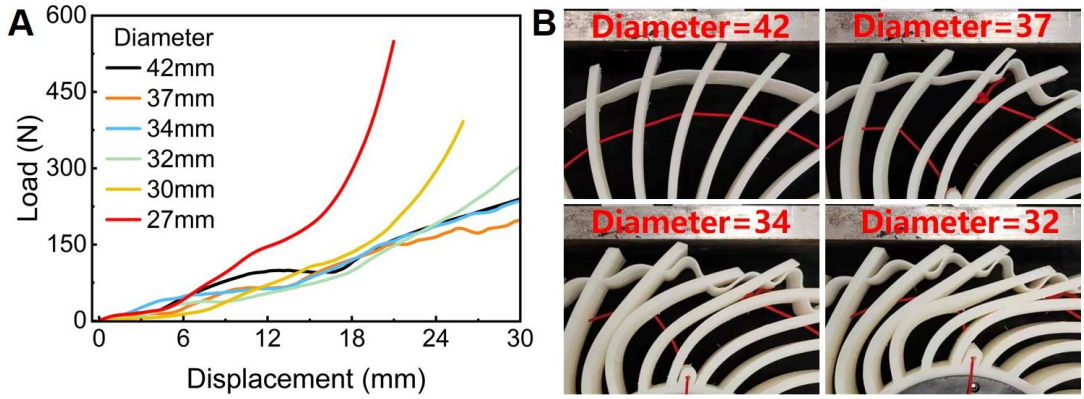

Supplementary Figure 16. Stiffness analysis and experiment of intermediate states of the flexible wheel. (A) The variation in radial stiffness of wheels with different diameters. (B) The schematic comparison of the gap between the spokes in the initial phase(Photographed by the authors).

Structural dimensions	Expanded state	Contracted state	Stiffness curve comparison
Mounting hole: 104mm Outer ring : 372mm	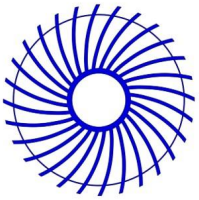	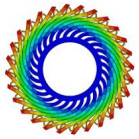	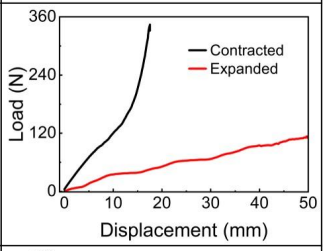
Mounting hole: 104mm Outer ring: 412mm	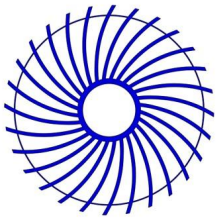	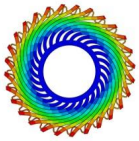	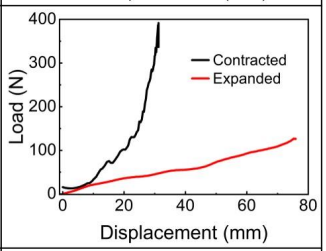
Mounting hole: 104mm Outer ring: 452mm	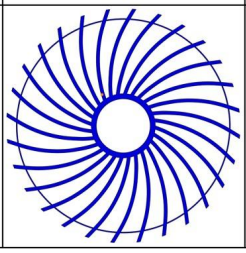	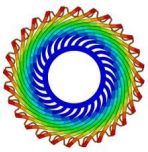	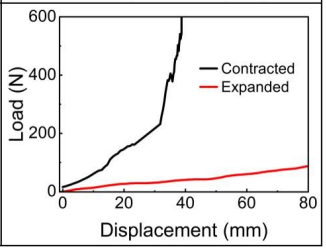

Supplementary Figure 17. The generalizability analysis of wheels with a 104mm mounting hole diameter.

Structural dimensions	Expanded state	Contracted state	Stiffness curve comparison
Mounting hole: 144mm Outer ring : 372mm	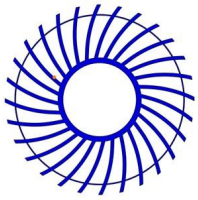	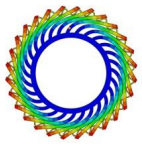	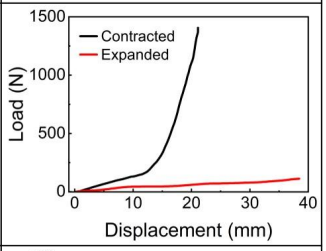
Mounting hole: 144mm Outer ring: 412mm	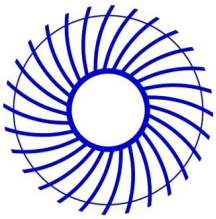	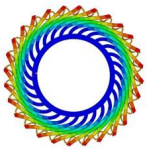	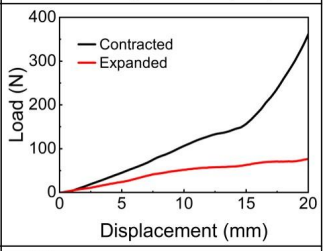
Mounting hole: 144mm Outer ring: 452mm	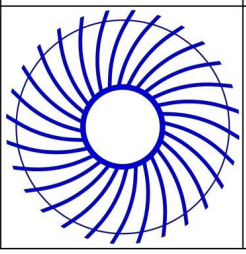	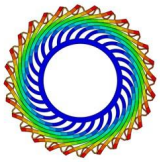	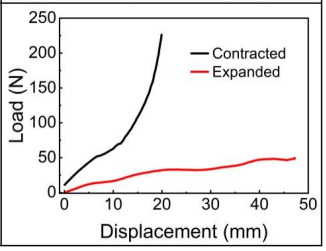

Supplementary Figure 18. The generalizability analysis of wheels with a 144mm mounting hole diameter.

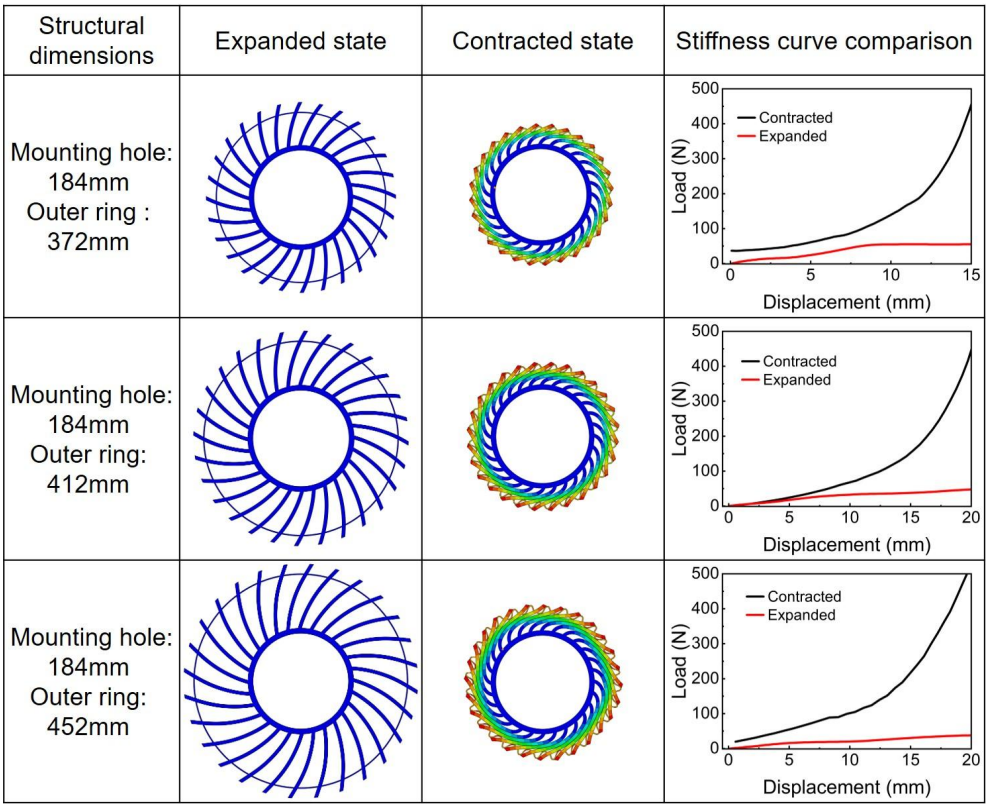

Supplementary Figure 19. The generalizability analysis of wheels with a 184mm mounting hole diameter.

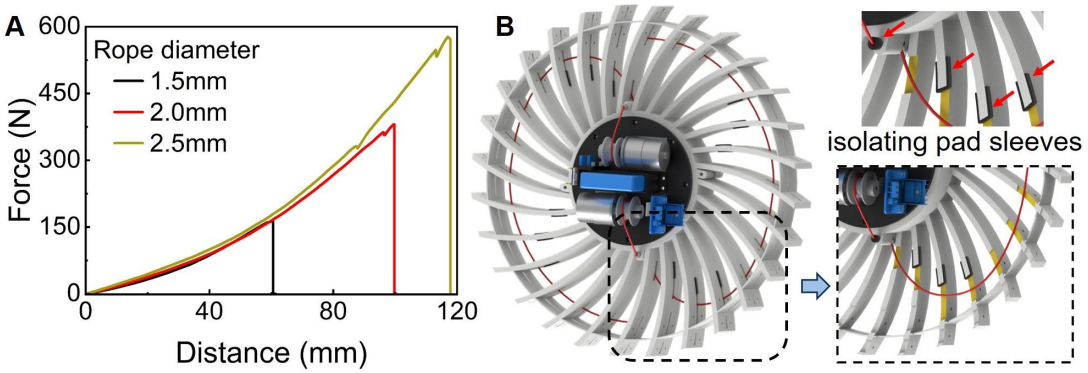

Supplementary Figure 20. Rope tension testing and the spatial distribution of ropes. (A) The relationship between tension and displacement during the rope stretching process. (B) The spatial trajectory distribution corresponding to the interaction between the rope and the wheel, along with the positioning of the isolating pad sleeves added to prevent excessive local wear.

Supplementary Table 1. Comparison of performance in existing robots

Ref	Type	n	T_{max} (N·m)	M_{robot} (kg)	H_{max} (m)	Obstacle-crossing capability	Maximum speed (m/s)
[9]	Rigid reconfigurable	2	2.16	1.50	0.28	0.95	0.32*
[10]	Rigid reconfigurable	2	1.40	2.00	0.12	0.84	0.94*
[11]	Rigid reconfigurable	2	1.20	1.23	0.10*	0.50	1.95*
[12]	Rigid reconfigurable	4	17.00	15.80	0.24	0.54	3.15
[13]	Rigid reconfigurable	4	3.04	2.80	0.23	0.52	0.53
[14]	Rigid reconfigurable	4	9.70	23.00*	0.10	0.58	0.72*
[15]	Rigid reconfigurable	4	24.50	13.00	0.22	0.29	0.30
[16]	Rigid reconfigurable	2	0.36	0.70	0.13	1.25	0.80
[17]	Flexible reconfigurable	4	4.30*	14.00*	0.18	1.44	0.83
[18]	Flexible reconfigurable	2	1.5e-3*	4.5e-3	0.02*	0.22	0.68
[19]	Flexible reconfigurable	2	0.50	0.28	0.05	0.14	0.20*
[20]	Non-reconfigurable	2	78.00	78.00	0.20	0.98	1.00*
[21]	Non-reconfigurable	4	0.50*	1.00*	0.08	0.41	1.00*
[22]	Non-reconfigurable	4	0.10*	0.30*	0.10*	0.74	0.13
This work	Flexible reconfigurable	2	9.60	22.00	0.13	1.66	2.50

The parameter calculations are directly based on the data provided in the paper. For data not explicitly given, inference is applied. For instance, the maximum driving torque and maximum travel speed are determined by referencing the motor model mentioned in the paper and querying the corresponding product performance specifications. With the motor performance parameters, the robot's ideal maximum speed can be inferred based on the motor's rated speed and the robot's wheel diameter [9,10,11,14,19,20,21]. The driving torque is then selected according to the motor's maximum output torque [17,18,21,22]. In the case of the maximum obstacle-crossing height, when not mentioned in the article, the wheel radius is used as a substitute [11,18,22]. Theoretically, when using wheel-based rolling, the maximum obstacle-crossing height is equal to the wheel radius. For the total robot mass, which is not explicitly mentioned, the paper typically provides the mass of a single modular wheel. The total robot mass is estimated by multiplying the wheel mass by the number of wheels and adding an estimated body mass [14,17,21,22], with the estimated weight rounded up to the maximum value based on real-world objects. (The data marked with an asterisk (*) in the table indicates values derived through inference)

Supplementary Table 2. Ground contact coefficients of the spiral wheel in two different states

Wheel status	**Grounding length (mm)**	**Grounding width (mm)**	**Grounding coefficient**	**Average pressure (Mpa)**	**Pressure skewness (Mpa)**
Expanded state	132.72	52	2.552	0.168	0.208
Contracted state	78.24	52	1.505	0.228	0.359

Supplementary Movie 1.
Radial Compression Test of the Spiral wheel in Its Expanded State: The spiral wheel is not contracted and is fixed onto the clamp of the testing machine. The compression rate of the machine is set to 5 mm/min.

Supplementary Movie 2.
Radial Compression Test of the Spiral wheel in Its Contracted State: The spiral wheel is first fixed onto the clamp and then contracted. The same compression rate as used in the expanded state is applied during this test.

Supplementary Movie 3.
Spiral wheel Contraction Test: The spiral wheel is fixed onto a clamp on the testing machine. Under the external tension of a fine rope, the spiral wheel contracts into a relatively round shape, resembling a compact wheel.

Supplementary Movie 4.
Bluetooth-Controlled Transition of the Spiral wheel from Expanded to Contracted State: The robot remains in an upright position. A command is sent from the control unit to initiate the contraction mechanism. Upon receiving the contraction command, the spiral wheel smoothly transitions from its expanded to contracted state, without affecting the robot's standing balance during the entire process.

Supplementary Movie 5.
Bluetooth-Controlled Transition of the Spiral wheel from Contracted to Expanded State: After the spiral wheel has contracted, a release command is sent from the control unit to the mechanism. Upon receiving this command, the spiral wheel smoothly transitions from its contracted to expanded state. Similarly, the robot's standing balance remains unaffected.

Supplementary Movie 6.
Robot Stair Climbing Test with Spiral wheel: The robot follows a stair climbing strategy controlled from the control unit. First, the spiral wheel makes contact with the stairs, followed by the robot's body tilting forward for a short distance. The robot then jumps, successfully overcoming the stairs. Thanks to the cushioning effect of the

spiral wheel, the robot can also descend the stairs smoothly, without any risk of tipping over during the descent.

Supplementary Movies 7 and 8.

Robot Traversing a Dirt Slope and Stone Path: The robot operates in the obstacle-crossing mode with the spiral wheel in its expanded state, successfully navigating a dirt slope and stone path.

Supplementary Movie 9.

Robot Traversing Grass Terrain: In the obstacle-crossing mode with the spiral wheel expanded, the robot can also navigate grass terrain without any issues.

Supplementary Movie 10.

Robot High-Speed Mode with Spiral wheel: When the spiral wheel is switched to high-speed mode (contracted state), the robot can travel at full speed smoothly, without any noticeable bouncing or instability during the movement.

Supplementary Movie 11.

Robot Traversing Wooden Stairs in the Park: Using its stair climbing strategy, the robot successfully climbs a wooden staircase in a park with steps approximately 12 cm high.

References

1. Ren J, Yuan H. Contact analysis and friction prediction of non-gaussian random surfaces. *Appl Sci*. 2022;12(21):11237. doi:10.3390/app122111237
2. Melly SK, Liu L, Liu Y, Leng J. A review on material models for isotropic hyperelasticity. *Int J Mech Syst Dyn*. 2021;1(1):71-88. doi:10.1002/msd2.12013
3. Petroudi AR, Afrasiab H, Hassani A. Peridynamic formulation for hyperelastic mooney–rivlin materials employing a novel strain energy density approach. *Thin Walled Struct*. 2026;218:113989. doi:10.1016/j.tws.2025.113989
4. Guo T, Liu J, Liang H, et al. Design and dynamic analysis of jumping wheel-legged robot in complex terrain environment. *Front Neurorobot*. 2022;16:1066714. doi:10.3389/fnbot.2022.1066714
5. Wilhelm A, Melek W, Huissoon J, et al. Dynamics of step-climbing with deformable wheels and applications for mobile robotics. In: *2007 IEEE/RSJ International Conference on Intelligent Robots and Systems*. IEEE; 2007:783-788. doi:10.1109/IROS.2007.4399601
6. Elementary mechanical analysis of obstacle crossing for wheeled vehicles | IEEE conference publication | IEEE xplore. Accessed April 1, 2026. https://ieeexplore.ieee.org/document/4543560
7. Theory of ground vehicles | wiley online books. Accessed April 1, 2026. https://onlinelibrary.wiley.com/doi/book/10.1002/9781119719984
8. Thomas G, Vantsevich VV. Wheel-terrain-obstacle interaction in vehicle mobility analysis. *Veh Syst Dyn*. 2010;48(sup1):139-156. doi:10.1080/00423111003690496
9. Bai L, Guan J, Chen X, Hou J, Duan W. An optional passive/active transformable wheel-legged mobility concept for search and rescue robots. *Rob Auton Syst*. 2018;107:145-155. doi:10.1016/j.robot.2018.06.005
10. Sun T, Xiang X, Su W, Wu H, Song Y. A transformable wheel-legged mobile robot: design, analysis and experiment. *Rob Auton Syst*. 2017;98:30-41. doi:10.1016/j.robot.2017.09.008
11. She Y, Hurd CJ, Su HJ. A transformable wheel robot with a passive leg. In: *2015 IEEE/RSJ International Conference on Intelligent Robots and Systems (IROS)*. 2015:4165-4170. doi:10.1109/IROS.2015.7353966
12. Xu Q, Xu H, Xiong K, Zhou Q, Guo W. Design and analysis of a Bi-directional transformable wheel robot trimode. In: *2021 IEEE/RSJ International Conference on Intelligent Robots and Systems (IROS)*. 2021:8396-8403. doi:10.1109/IROS51168.2021.9636421

13. Chou JJ, Yang LS. Innovative design of a claw-wheel transformable robot. In: *2013 IEEE International Conference on Robotics and Automation*. 2013:1337-1342. doi:10.1109/ICRA.2013.6630744

14. Lee Y, Ryu S, Won JH, Kim S, Kim HS, Seo T. Modular two-degree-of-freedom transformable wheels capable of overcoming obstacle. *IEEE Robot Autom Lett*. 2022;7(2):914-920. doi:10.1109/LRA.2021.3096223

15. Zheng C, Sane S, Lee K, Kalyanram V, Lee K. WaLTR: adaptive wheel-and-leg transformable robot for versatile multiterrain locomotion. *IEEE Trans Robot*. 2023;39(2):941-958. doi:10.1109/TRO.2022.3226114

16. Kim YS, Jung GP, Kim H, Cho KJ, Chu CN. Wheel transformer: a wheel-leg hybrid robot with passive transformable wheels. *IEEE Trans Robot*. 2014;30(6):1487-1498. doi:10.1109/TRO.2014.2365651

17. Lee JY, Han S, Kim M, et al. Variable-stiffness–morphing wheel inspired by the surface tension of a liquid droplet. *Sci Rob*. 2024;9(93):eadl2067. doi:10.1126/scirobotics.adl2067

18. Lai Y, Zang C, Luo G, et al. An agile multimodal microrobot with architected passively morphing wheels. *Sci Adv*. 2024;10(51):eadp1176. doi:10.1126/sciadv.adp1176

19. Lee DY, Kim SR, Kim JS, Park JJ, Cho KJ. Origami wheel transformer: a variable-diameter wheel drive robot using an origami structure. *Soft Rob*. 2017;4(2):163-180. doi:10.1089/soro.2016.0038

20. Kim G, Chung H, Cho BK. MOBINN: stair-climbing mobile robot with novel flexible wheels. *IEEE Trans Ind Electron*. 2024;71(8):9182-9191. doi:10.1109/TIE.2023.3319739

21. Godden T, Mulvey BW, Redgrave E, Nanayakkara T. PaTS-wheel: a passively-transformable single-part wheel for mobile robot navigation on unstructured terrain. *IEEE Robot Autom Lett*. 2024;9(6):5512-5519. doi:10.1109/LRA.2024.3389828

22. Sun J, Lerner E, Tighe B, Middlemist C, Zhao J. Embedded shape morphing for morphologically adaptive robots. *Nat Commun*. 2023;14(1):6023. doi:10.1038/s41467-023-41708-6